The Journal of Adhesion

ISSN: (Print) (Online) Journal homepage: https://www.tandfonline.com/loi/gadh20

Analytical and numerical results for the elasticity and adhesion of elastic films with arbitrary Poisson's ratio and confinement

Christian Müller & Martin H. Müser

To cite this article: Christian Müller & Martin H. Müser (2022): Analytical and numerical results for the elasticity and adhesion of elastic films with arbitrary Poisson's ratio and confinement, The Journal of Adhesion, DOI: 10.1080/00218464.2022.2038580

To link to this article: https://doi.org/10.1080/00218464.2022.2038580

Published online: 27 Feb 2022.

THE JOURNAL OF ADHESION
https://doi.org/10.1080/00218464.2022.2038580

Taylor & Francis
Taylor & Francis Group

Analytical and numerical results for the elasticity and adhesion of elastic films with arbitrary Poisson's ratio and confinement

Christian Müller[a] and Martin H. Müser[a,b]

[a]INM - Leibniz Institute for New Materials, Saarbrücken, Germany; [b]Department. Of Materials Science and Engineering, Saarland University, Saarbrücken, Germany

ABSTRACT

We present an approximate, analytical treatment for the linearly elastic response of a film with arbitrary Poisson's ratio ν, which is indented by a flat cylindrical punch while resting on a rigid foundation. Our approach is based on a simple scaling argument allowing the vast changes of the elastomer's effective modulus $\bar{E}$ with the ratio of film height h and indenter radius a to be described with a compact, analytical expression. This yields exact asymptotics for large and small reduced film heights h/a, whereby it also reproduces the observation that $\bar{E}(h/a)$ has a pronounced minimum for $\nu > 0.49$ at $h/a \approx 1.6$. Using Green's function molecular dynamics (GFMD), we demonstrate that the predictions for $\bar{E}(h/a)$ are reasonably correct and generate accurate reference data for effective modulus and pull-off force. GFMD also reveals that the nature of surface instabilities occurring during stable crack growth as well as the crack initiation itself depend sensitively on the way how continuum mechanics is terminated at small scales, that is, on parameters beyond the two dimensionless numbers h/a and ν defining the continuum problem.

ARTICLE HISTORY
Received 22 October 2021
Accepted 29 November 2021

KEYWORDS
Adhesion; crack propagation; elastomer; modeling; theory; thin films

1. Introduction

This paper revisits the contact mechanics of confined, linearly elastic layers of height h sandwiched between a rigid surface and a circular rigid punch of radius a. A central quantity of such films is the effective modulus $\bar{E}$ [1] as a function of the reduced height h/a and the Poisson's ratio ν. $\bar{E}$ is defined as the ratio of mean contact stress and relative height change. The arguably most important reason for wanting to know $\bar{E}(h/a)$ is that it allows the pull-off stress $\sigma_p \leq$ [2,3] and the fracture mechanisms of confined elastomers to be determined.[4–8] For large h/a or small ν, adhesive contact failure is sudden, *i.e.*, the tensile force drops discontinuously from its maximum value to zero under quasi-static loading, even when the system is displacement driven. However, stable crack growth occurs for (nearly) incompressible elastomers

CONTACT Martin H. Müser martin.mueser@mx.uni-saarland.de INM - Leibniz Institute for New Materials, 66123 Saarbrücken, Germany

once h/a falls below approximately two. As h/a drops below unity, the contact shape is no longer circular during stable crack growth but clearly symmetry broken[4,6–9] so that contact features have a characteristic linear dimension λ minimizing the total energy.[4,8,10–13]

The limits of unconfined ($h/a \to \infty$)[14] and incompressible ($\nu = 0.5$), highly confined ($h/a \to 0$)[15] elastomers were solved more than half a century ago. Over time, amendments to the latter case were made with respect to boundary conditions, the geometry of the elastomer, and other details.[1,4,12,16] However, intermediate confinements $h/a \approx 1$ have not yet been solved analytically for extended two-dimensional films, although solutions for poker-chip specimens[17,18] as well as elastomeric strips[19] can be found. Extended films have only been treated numerically with finite-element (FE) simulations,[2,3,5,7,20,21] which lead to the suggestion of semi-empirical relationships between $\bar{E}/E^*$ and h/a,[3,5,20] where $E^* = E/(1-\nu^2)$ is the contact modulus and E the Young's modulus. They turn out to benefit the interpretation of real-laboratory experiments, in particular, to explain different crack propagation mechanisms during detachment.[4,6–8] A deeper understanding of the $\bar{E}(h/a)$ dependence might also prove useful in interpreting observations made on confined elastomers in contact with rough indenters.[22–24]

Unfortunately, most existing semi-empirical $\bar{E}(h/a)$ relations were only designed for Poisson's ratios equal to or just below 0.5 so that confinement effects of various soft materials with small Poisson's ratios, such as foams, corks or soft isotropic metamaterials with negative Poisson's ratio are not quantitatively understood. Moreover, as demonstrated in this work, the extreme confinement limit, in which deviations from ideal incompressible matter have not yet been described satisfactorily for the given elastic film geometry. While instabilities of the elastomer surface were studied analytically for arbitrary Poisson's ratios,[10,25] the focus was quickly laid on ideally incompressible elastomers.[10,12,21] In addition, no physically motivated, closed-form expressions for the dependence of the effective modulus on the reduced film height have been proposed.

The original main motivation for this article was to identify a non-empirical relationship for $\bar{E}(h/a, \nu)$, which allows us to easily rationalize the minimum in $\bar{E}(h/a, \nu)$ and estimate the range of Poisson's ratios, in which an elastomer film behaves as if it were incompressible. To this end, we propose that the energy needed to deform the elastic film should be most sensitive to the stiffness of a surface undulation with a wavevector in the order of the inverse punch radius. Even if such a simple scale argument may not outperform existing, more empirical models for all possible combinations of h/a and ν, it should improve our

ability to estimate $\bar{E}(h/a, \nu)$, in particular in the limit of extreme confinement and/or small Poisson's ratio. It certainly behoves us to examine numerically the accuracy of any scaling relation, which we do by running Green's function molecular dynamics (GFMD) simulations.[26] This also allows us to produce reference data for the pull-off stress as a function of h/a and ν. While simulating the detachment process, we realized that the analysis of surface instabilities that occur during stable crack growth at $h/a \lesssim 1$ is interesting in its own right. We therefore include an in-depth analysis of how substrate symmetry, lattice trapping, and stochastic irregularities in the form of thermal noise, as well as their interplay affect the patterns that occur when the surface morphology becomes unstable during detachment.

The remainder of this article is organized as follows: Model and numerical methods are introduced in Section 2. Our scaling approach is presented in Section 3. Section 4 contains a comparison between theory and simulations as well as additional simulation results. Conclusions are drawn in Section 5.

2. Model and methods

2.1. Model

The investigated model system consists of isotropic, linearly elastic films of varying film height h resting on a perfectly flat and perfectly rigid foundation with a surface normal in the z direction. The in-plane extent of film and foundation are taken to be infinitely large and a no-slip condition is assumed between them. The opposite surface of the elastomer interacts with a rigid circular punch of radius a through a hard-wall constraint with a slip condition. Such systems can be effectively simulated by assuming periodic boundary conditions in the xy plane, as long as the linear dimension L of the periodically repeated simulation cell exceeds the punch radius a by a sufficiently large padding, which is most effectively chosen to be larger than but of order $\min(h, a)$.

In the just-defined setup, the elastic energy of the elastomer is given by[27–29]

$$V_{\mathrm{ela}} = \sum_{\mathbf{q}} \frac{qE^*}{4} c(\nu, qh) |\tilde{u}(\mathbf{q})|^2 \tag{1}$$

where $\mathbf{q}$ is an in-plane wave vector with absolute value q, $\tilde{u}(\mathbf{q})$ is the Fourier coefficient of the displacement field of the elastomer's surface facing the indenter and

$$c(\nu, qh) = \frac{(3-4\nu)\cosh(2qh) + 2(qh)^2 - 4\nu(3-2\nu) + 5}{(3-4\nu)\sinh(2qh) - 2qh}. \tag{2}$$

For an infinitely large system without periodic boundaries, the sum on the r.h.s. of Eq. (1) will be replaced with an appropriate integral. For some of the calculations presented in this study, knowledge of the asymptotes of $c(\nu, qh)$ is useful. A Taylor expansion reveals them to be

$$c(\nu, qh) = \begin{cases} 1 & \text{for } qh \gg 1 \\ c_1(\nu)/(qh) & \text{for } qh \ll 0.5 - \nu \quad \text{and } \nu < 0.5 \\ 1.5/(qh)^3 & \text{for } qh \ll 1 \quad \text{and } \nu = 0.5. \end{cases} \tag{3}$$

with

$$c_1(\nu) = \frac{2(1-\nu)^2}{1-2\nu}. \tag{4}$$

In our analytical treatment, the interaction between indenter and elastomer is a non-overlap constraint. In addition, a surface energy γ is gained per unit area where surfaces touch. The model is then replaced with a cohesive zone model for the numerical solution of the contact problem, which is described next.

2.2. Methods

The contact problems were solved numerically using Green's function molecular dynamics (GFMD) simulations.[26] GFMD is a boundary-value method, in which Newton's equations of motion for the displacement fields are solved in their Fourier representation. In compression simulations, we use an exact non-overlap constraint in conjunction with the fast-inertial relaxation (FIRE)[30] algorithm as described in Ref.[31] Typical simulations assume the linear dimension of the periodically repeated simulation cell to be three times the punch diameter and a discretization of the displacement field into $2,048 \times 2,048$ elements. While exploiting the circular symmetry of the problem would have allowed us to reduce the computational cost of the simulations substantially, we found it more time effective to use the implemented methods.

Although knowledge of V_{ela} as a function of normal displacement and h/a determined from purely repulsive experiments is sufficient to deduce the adhesive pull-off force, see Section 3.3, simulations mimicking tensile loading were also conducted. This was not only done to double-check our pull-off force calculations but also to investigate the dynamics and failure mechanisms that occur during the detachment of confined elastomers. For this purpose, adhesion is modeled with a cohesive zone model (CZM), in which the gap-dependent surface energy has the form[32]

$$\gamma(g) = -\gamma \times \begin{cases} \{\cos(kg) + 1\}/2 & \text{for } 0 \le kg \le \pi/\Delta a \\ \{1 - (kg)^2/4\} & \text{for } g < 0 \end{cases} \tag{5}$$

and zero else, where g is the gap between elastomer and punch. The parameter k was generally set such that the maximum stiffness of surface undulations was slightly more than twice the maximum (negative) curvature of the potential defining the CZM, *i.e.*, $k^2 = \frac{0.4}{r} q_{\max} E^* c(\nu, q_{\max} h)$, where $q_{\max} = \sqrt{2}\pi/\Delta a$ and Δa the linear mesh discretization. In this way, the interaction is effectively as short ranged as possible while avoiding lattice trapping. The latter refers to a situation, where an individual degree of freedom, *e.g.*, a GFMD discretization point, can have two or more mechanically stable positions, while all other points remain fixed. When addressing lattice trapping, the parameter k was set to 3.75 times its default value. To improve the convergence rate, the mass-weighting GFMD variant was used for adhesive simulations.[31] Computing time is furthermore reduced by progressively increasing spatial resolution and decreasing the rate of retraction upon approaching the point of maximum tensile force.

To also model the response of elastomers to small perturbations, some simulations were conducted at finite temperature with the help of a recently introduced GFMD thermostat.[33] To this end, the thermal energy was kept at about 0.1% of the adhesive energy gained in a single mesh element in which the elastomer makes perfect contact with the indenter.

2.2.1. Finite-size corrections

If the origin of the coordinate system coincides with the center of the flat punch, the macroscopic displacement u_0 is defined as $u(0) - u(r \to \infty)$. Thus, the best simple estimate for u_0 when using a finite square-shaped simulation cell with length L is to replace $u_\infty \equiv u(r \to \infty)$ with $u(L/2, L/2)$.

To reduce the finite-size error, we use a correction appropriate for semi-infinite elastomers[34] but damp it with the weight function $w(h/a) = \tanh(h/a)$ for small h/a:

$$u_\infty \approx u(L/2, L/2) + 5\, w(h/a)\{u(L/2, L/2) - u(L/2, 0)\}. \tag{6}$$

The damping of the usual correction is needed because for finite h/a, the displacement field approaches u_∞ exponentially quickly with increasing distance r from the origin rather than with $1/r$.

3. Theory

As has been done before,[2,3,35] we define the effective modulus $\bar{E}$ as the ratio of the mean (compressive) contact stress $\bar{\sigma} = F/(\pi a^2)$ and the relative height change of the elastomer to the contact area, $\bar{\varepsilon} = u_0/h$, even if the uncompressed elastomer is a film rather than a free-standing cylinder of radius a, for

which $\bar{E}$ was originally introduced.[35] Here, u_0 is the normal displacement of the elastomer's surface right below the punch from its equilibrium height in the absence of an indenter. Thus, $\bar{E}$ is given by

$$\bar{E} = \frac{\bar{\sigma}}{\bar{\varepsilon}} = \frac{Fh}{u_0 \pi a^2}. \tag{7}$$

Since a does not change with u_0 for a flat punch under compression, it follows that F is proportional to u_0 within linear elasticity. Thus, the elastic energy is simply given by $V_{\mathrm{ela}} = Fu_0/2$ so that

$$V_{\mathrm{ela}} = \left(\pi a^2\right) \frac{\bar{E}}{2h} u_0^2. \tag{8}$$

As already argued in the introduction, the only in-plane length defining the contact problem is the punch radius a. Thus, under compression, dimensional analysis suggests that the elastic energy should predominantly reside in undulations with wave numbers of the order of $q_a = 2\pi/a$ given that $q \to 0$ or $q \to \infty$ modes are not dominant. In this case, a good estimate for the elastic energy would be

$$V_{\mathrm{ela}} = \left(\pi a^2\right) \mathcal{O}(q_a) E^* c\{\nu, \mathcal{O}(q_a)h\} u_0^2. \tag{9}$$

In order to eliminate the big-O notation in Eq. (9), we introduce two proportionality factors α and β. Comparing the resulting elastic energy to Eq. (8) yields

$$\frac{\bar{E}}{E^*} \approx \frac{1}{2} \alpha\beta q_a h\, c\{\nu, \beta q_a h\}, \tag{10}$$

which is the central analytical result of this work. Sections 3.1 and 3.2 are concerned with a parametrization of α and β, while Section 3.3 summarizes how to deduce depinning forces from the h/a dependence of $\bar{E}$.

To further motivate our approach, Figure 1 shows displacement and stress fields in real space for the various confinements, which range from small ($h/a \gg 1$) and intermediate ($h/a = 1$) via large ($1 - 2\nu \ll (h/a)^2 \ll 1$) to extreme ($(h/a)^2 \ll 1$). These data are complemented by the elastic energy associated with individual $\tilde{u}(\mathbf{q})$ modes in the right column of Figure 1, which clearly supports the scaling hypothesis that energy predominantly resides in modes with wavelengths of order a.

The top row of Figure 1 shows the well-established properties of the flat-punch solution for semi-infinite elastomers. On the other end, in the two bottom rows, Figure 1 reveals a qualitative difference between large and extreme confinement, which may often be underappreciated, although the principle is known from works addressing poker-chip and

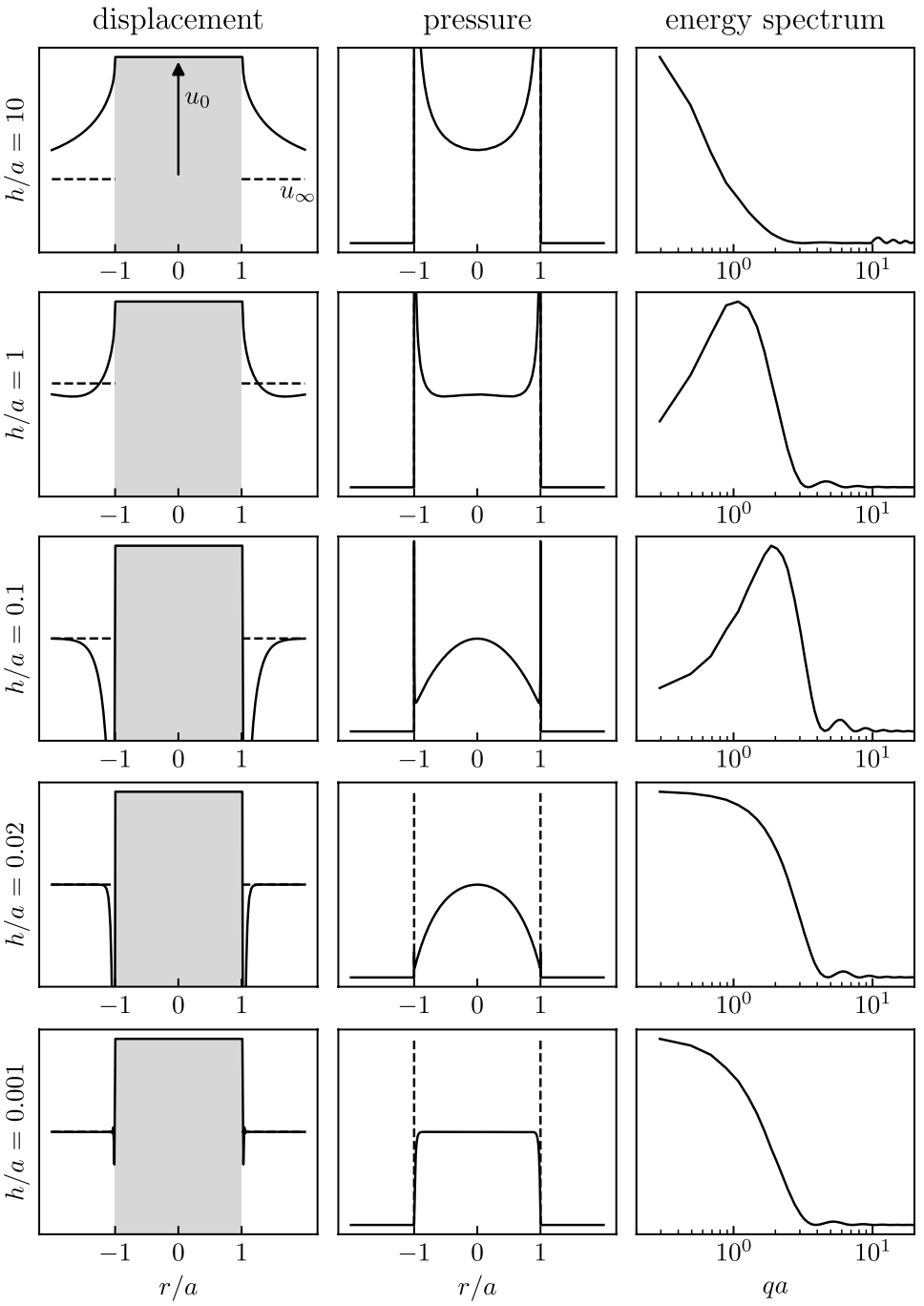

Figure 1. Displacement field (left column), stress field (center column), and energy spectrum (right column), *i.e.*, individual summands of the r.h.s. of Eq. (1), for $\nu = 0.4995$ at different values of the reduced height h/a. The ordinate axis is linear in all cases.

elastic-strip geometries.[17–19] Specifically, for $1-2\nu<(h/a)^2\ll 1$, the stress profile at the origin is close to an inverted parabola while for $(h/a)^2\ll 1-2\nu$, the stress is constant within (most of) the contact. It should also be noted that in all cases, a stress singularity occurs at the contact edge, which in our numerical treatment – and in reality – is cut off by the finite range of the interaction potential, whose precise effective value can be a function of the microscopic roughness.[33] In addition, the corresponding intensity decreases with decreasing h/a and thus disappears in the limit of $h/a\to 0$.

3.1. Asymptotic scaling

In many cases, nearly incompressible elastomers are treated as perfectly incompressible and their Poisson's ratio is approximated with $\nu=0.5$.[4–6,35] However, analyzing the asymptotic behavior of $\bar{E}$ for $h/a\to 0$ reveals a more concise picture, which is presented in the following.

The ratio $\bar{E}/E^*$ can only be a function of the two dimensionless numbers defining the problem, namely ν and h/a. The asymptotic limits for $\bar{E}/E^*$ at extreme and small confinement can be deduced from existing solutions for the considered confined elastomer. As will be shown in the remaining part of this Section 3.1, they turn out to be

$$\frac{\bar{E}}{E^*}=\begin{cases}2h/(\pi a) & \text{for } h/a\gg 1\\ c_1(\nu)/2 & \text{for } h/a\ll\sqrt{1-2\nu} \quad \text{and } \nu<0.5\\ 3a^2/(32h^2) & \text{for } h/a\ll 1 \quad \text{and } \nu=0.5,\end{cases} \tag{11}$$

where $c_1(\nu)$ was introduced in Eq. (4).

The condition $(h/a)^2\ll 1-2\nu$ for $\nu<0.5$ in Eq. (11) is motivated by the observation that for ν close to 0.5, the scaling of the function $c(\nu,h/a)$ has two different small-h/a scaling regimes. The threshold between these regimes is characterized by the transition from a parabolic to a constant stress distribution as illustrated by Figure 1. Based on this we introduce the terminology that a film is extremely confined if h/a is small compared to $\sqrt{1-2\nu}$ and largely confined if this condition does not hold but h is still small compared to a.

3.1.1. Unconfined limit

The unconfined limit is nothing but a regular flat punch in contact with a semi-infinite half space.[14] Inserting its well-known stress–displacement relation $F=2aE^*u_0$ into Eq. (7) yields the first case given in Eq. (11).

3.1.2. Extreme confinement limit

For $h/a \to 0$ and $\nu < 0.5$, the proportionality between the elastic energy of a single height undulation and $|\tilde{u}(\mathbf{q})|^2$ does not depend noticeably on the wave number q. Due to Parseval's theorem, a linear relation between local displacement and local stress occurs within most of the contact. This is why the stress is approximately constant within the contact in the bottom row of Figure 1 and zero outside so that its Fourier transform is

$$\tilde{\sigma}(\mathbf{q}) = \frac{\bar{\sigma}}{2\pi}\int \mathrm{d}^2 r\, e^{i\mathbf{q}\cdot\mathbf{r}}\,\Theta(a-r) \tag{12}$$

$$= \bar{\sigma} a J_1(aq)/q, \tag{13}$$

$\Theta(\ldots)$ being the Heaviside step function, $\mathbf{r} = (x, y)$ the in-plane position with $r = |\mathbf{r}|$ and $J_n(\ldots)$ the Bessel function of the first kind of order n. Using the stress–strain relation that follows from Eq. (1) yields a displacement at the origin $u_0 \equiv u(r = 0)$ of

$$u_0 = \frac{1}{2\pi}\int \mathrm{d}^2 q\, \frac{a}{q} J_1(aq)\, \frac{2}{q\, c(\nu, qh)}\, \frac{\bar{\sigma}}{E^*} \tag{14}$$

$$\Rightarrow \frac{u_0/h}{\bar{\sigma}} = \frac{2}{\tilde{h} E^*}\int_0^\infty \mathrm{d}\tilde{q}\, \frac{J_1(\tilde{q})}{\tilde{q}\, c\left(\nu, \tilde{q}\tilde{h}\right)}, \tag{15}$$

where $\tilde{h} = h/a$ is the reduced height and $\tilde{q} = qa$. By definition, the l.h.s. of Eq. (15) and thus its r.h.s. is nothing but the inverse of the effective elastic modulus $\bar{E}$.

The integral on the r.h.s. of Eq. (15) probably has no closed-form analytical solution and is even difficult to solve numerically because of the oscillations of the Bessel function. To reduce the effect of the oscillations, we rewrite the integral as

$$I = \int_0^\infty \mathrm{d}\tilde{q}\, \frac{f(\tilde{q}) + f(\tilde{q}+\pi)}{2} + \frac{1}{2}\int_0^\pi \mathrm{d}\tilde{q} f(\tilde{q}), \tag{16}$$

$f(\tilde{q})$ being the integrand on the r.h.s. of Eq. (15). In its rewritten form, the integral can be easily seen to have its dominant contribution from small $\tilde{q}$ when $\tilde{h}$ is small. This property does not change after using the appropriate small-$\tilde{q}$ approximation for $c(\nu, \tilde{q})$ in the integrand. As a consequence, I can be solved analytically to be $\tilde{h}/c_1(\nu)$ in the large-confinement limit for $\nu < 0.5$, which ultimately translates into the corresponding expression stated in Eq. (11).

3.1.3. Large-confinement limit

For $\nu = 0.5$ and h sufficiently small compared to a, or, alternatively, $\nu < 0.5$ and h/a in the intermediate scaling regime, the stiffness of a mode is no longer independent of q but instead proportional to q^{-2}. As a consequence, the stress is no longer constant in the contact area but assumes the functional form[35]

$$\sigma(r) = \sigma_0 \left(1 - r^2/a^2\right) \Theta(a - r) \tag{17}$$

with $\sigma_0 = 2\bar{\sigma}$, see also the second to last row in Figure 1. It should be noted that this stress distribution was originally derived for a finite elastomer of originally cylindrical shape sandwiched between two rigid planes and assuming a stick condition. However, Gent[35] already expected the functional dependence of $\bar{E}$ on h/a for his set-up to be similar to that of films.

Proceeding as in Section 3.1.2, we first determine $\tilde{\sigma}(\mathbf{q})$ to be

$$\tilde{\sigma}(\mathbf{q}) = \int_0^a \mathrm{d}r\, r J_0(qr)\sigma(r) = \sigma_0 a^2 \left(\frac{J_1(\tilde{q})}{\tilde{q}} - 2\frac{J_2(\tilde{q})}{\tilde{q}^2} + \frac{J_3(\tilde{q})}{\tilde{q}}\right). \tag{18}$$

The displacement in the origin then becomes

$$u_0 = \frac{2a\sigma_0}{E^*} \int_0^\infty \mathrm{d}\tilde{q}\, \frac{1}{c(\nu, \tilde{q}\tilde{h})} \left(\frac{J_1(\tilde{q})}{\tilde{q}} - 2\frac{J_2(\tilde{q})}{\tilde{q}^2} + \frac{J_3(\tilde{q})}{\tilde{q}}\right) \tag{19}$$

$$\overset{\text{Eq.(3)}}{\Rightarrow} \frac{u_0/h}{\bar{\sigma}} = \frac{8\tilde{h}^2}{3E^*} \int_0^\infty \mathrm{d}\tilde{q} \left(\tilde{q}^2 J_1(\tilde{q}) - 2\tilde{q} J_2(\tilde{q}) + \tilde{q}^2 J_3(\tilde{q})\right). \tag{20}$$

As in the previous section, the integral cannot be solved analytically and the integrand oscillates too much to allow for a numerically robust integration. We therefore proceed again as described in the text around Eq. (16). This time, we did not identify a closed-form expression for the small-q expansion, but found a numerical value of 4 with six significant digits, so that we believe 4 to be the exact value for the integral on the r.h.s. of Eq. (20). Thus, comparing the r.h.s. of Eq. (20) with the definition of $\bar{E}$ yields the large-confinement limit for $\bar{E}$ and $\nu = 0.5$.

3.2. Intermediate reduced film heights

In the previous section, we derived the asymptotic dependence of $\bar{E}$ on h/a at large and small h/a. We now want to ascertain how to chose α and β. To this end, we define $\tilde{E}_\mathrm{s} = \bar{E}_s/E^*$ as the r.h.s. of Eq. (10). Inserting the asymptotes of $c(\nu, qh)$ from Eq. (3) into Eq. (10) yields

$$\frac{\bar{E}_\mathrm{s}}{E^*} = \begin{cases} \alpha\beta q_a h/2 & \text{for } h/a \gg 1 \\ c_1(\nu)\alpha/2 & \text{for } h/a \ll \sqrt{1-2\nu} \quad \text{and } \nu < 0.5 \\ 3\alpha/\left\{4\beta^2 (q_a h)^2\right\} & \text{for } h/a \ll 1 \quad \text{and } \nu = 0.5. \end{cases} \tag{21}$$

Comparing this result to Eq. (11) reveals that $\bar{E}_s$ scales properly with h/a in the asymptotic limits. However, when expressing the elastic energy of the system and the subsequent effective modulus, there are three equations and just two parameters

$$\alpha\beta = 2/\pi^2 \qquad \text{for any } \nu \tag{22a}$$

$$\alpha = 1 \qquad \text{for } \nu < 0.5 \tag{22b}$$

$$\alpha\beta^{-2} = \pi^2/2 \qquad \text{for } \nu = 0.5. \tag{22c}$$

Thus, Eqs. (22b) and (22c) give conflicting optimum parameter choices for $\nu < 0.5$ and $\nu = 0.5$. They are $\alpha = 1$, $\beta = 2/\pi^2$ for $\nu < 0.5$ and $\alpha = 2/\pi$, $\beta = \sqrt[3]{4/\pi^4}$ for $\nu = 0.5$.

An exact representation of $\bar{E}(h/a)/E^*$ may be achievable by adding (infinitely) many summands as they occur on the r.h.s. of Eq. (10). To make these sums satisfy the asymptotic limits, Eq. (22) must be generalized to sum rules. However, we did not find that proceedings along those lines appeared to be promising. Therefore, we will only use the single wave-number, asymptotically correct approximations for $\bar{E}(h/a)$.

3.3. Deducing depinning force and range of stable crack growth from the effective modulus

Refs.[3–6,8] relate $\bar{E}(h/a)$ (or its inverse) to the energy release rate G, from which the pull-off force and crack propagation dynamics can be deduced. Similar to Yang and Li,[36] we start from the total energy formulation rather than the energy release rate, as we find this more direct and more intuitive.

The total potential energy of our system in an externally potential producing a constant force F reads

$$U = \frac{\bar{E}(h/a_c)}{2}\left(\frac{u_0}{h}\right)^2(\pi h a_c^2) - \pi a_c^2\gamma - Fu_0, \tag{23}$$

where a negative value of F implies a (positive) tensile force causing a negative displacement u_0. In this nomenclature, a_c is the actual contact radius, which may now be different from the punch radius a.

In equilibrium, u_0 and contact radius a_c both minimize the potential energy, *i.e.*, $\partial U/\partial a = \partial U/\partial u_0 = 0$. In stable equilibrium, the Hessian produced by the second-order derivatives of U w.r.t. u_0 and a_c must be positive definite. When the system is displacement-driven, this condition reduces to $\partial^2 U/\partial a_c^2 > 0$.

The generalized force acting on the radius a_c, $F_a \equiv -\partial U/\partial a_c$, is easily deduced as

$$F_a = 2\pi\gamma a_\mathrm{c} - \pi\bar{E}(h/a_\mathrm{c})\frac{u_0^2}{h}a_\mathrm{c} + \frac{\pi}{2}\frac{\partial\bar{E}(h/a_\mathrm{c})}{\partial a_\mathrm{c}}\frac{u_0^2 a_\mathrm{c}^2}{h}. \tag{24}$$

This equation allows a_c to be determined self-consistently for a given u_0. However, it has to be kept in mind that a_c cannot grow for positive F_a when a_c is equal to the punch radius a. This is why the case of $a_\mathrm{c} = a$ and $a_\mathrm{c} < a$ must be treated separately.

The contact radius starts shrinking when $F_a(u_0, a_\mathrm{c} = a) = 0^-$ on retraction. Inserting this condition into Eq. (24) and solving for u_0 yields

$$u_0 = -\sqrt{\frac{4\gamma h}{2\bar{E}(h/a_\mathrm{c}) + a_\mathrm{c}\partial\bar{E}(h/a_\mathrm{c})/\partial a_\mathrm{c}}}, \tag{25}$$

which has to be evaluated at $a_\mathrm{c} = a$ to deduce the normal displacement at the point, where the contact is just about to start shrinking for the first time. The normal force acting on the punch can then be deduced from $\partial U/\partial u_0 = 0$ to be

$$F(a_\mathrm{c}) = -\sqrt{\frac{4\bar{E}(h/a_\mathrm{c})\gamma/h}{2 + \partial\ln\bar{E}(h/a_\mathrm{c})/\partial\ln a_\mathrm{c}}}\pi a_\mathrm{c}^2. \tag{26}$$

Evaluating this force at $a_\mathrm{c} = a$ gives the depinning or pull-off force $F_p \equiv -F(a)$, which is the maximum tensile force occurring right before the contact radius starts shrinking. Different representations of the same equation can also be found using the energy release rate and/or assuming the load-driven case.[2,16]

As mentioned above, the previously determined contact radius a_c is only stable if $\partial^2 U/\partial a_c^2 > 0$, which can be written in a convenient form that reproduces $\partial U/\partial a_c$, which is 0 in equilibrium:

$$\frac{\partial^2 U}{\partial a_c^2} = \frac{1}{a_c}\frac{\partial U}{\partial a_c} + \frac{\pi u_0\bar{E}}{2h}\left(\frac{\partial^2\ln\bar{E}}{(\partial\ln a_c)^2} + \left(\frac{\partial\ln\bar{E}}{\partial\ln a_c}\right)^2 + 2\frac{\partial\ln\bar{E}}{\partial\ln a_c}\right) > 0. \tag{27}$$

The dividing line between stable and unstable crack propagation is defined by the condition $\partial F_a/\partial a_\mathrm{c} = 0$. It can be cast

$$\frac{\partial^2\ln\bar{E}(h/a_c)}{(\partial\ln a_c)^2} + \left(\frac{\partial\ln\bar{E}(h/a_c)}{\partial\ln a_c}\right)^2 + 2\frac{\partial\ln\bar{E}(h/a_c)}{\partial\ln a_c} = 0. \tag{28}$$

This criterion together with Eq. (21) can be used to explain why there is no stable crack growth in an adhesive contact between a flat punch and a semi-infinite elastomer. For confined bodies, especially when ν is close to 0.5, this procedure is no longer applicable, since the contact area is usually not circular.

4. Results and discussion

4.1. Effective modulus

Figure 2 compares numerical results for $\bar{E}/E^*$ to the analytical results from the previous section using adjustable parameters α and β following from Eq. (22). It is shown that the simple scaling approach reproduces the overall trends fairly well. By design, the asymptotic limits are matched for $\nu < 0.5$. Moreover, the location of the minimum in $\bar{E}(h/a)/E^*$, so it exists for a given Poisson's ratio, almost coincides between theory and simulation. However, the value of $\bar{E}/E^*$ in the minimum has an error of a few 10%. Errors are largest in the regime where a $\nu \lesssim 0.5$ elastomer shows similar behavior to an ideally incompressible solid. This can be rationalized by the $h/a \to 0$ asymptotics of a $\nu = 0.5$ body, which would require the parameters α and β to be redefined. For reasons of completeness, we note that the minimum of $\bar{E}(h/a)/E^*$ for $\nu = 0.5$ is located at $h/a = 1.665$ in our analytical treatment and at $h/a \approx 1.23 \pm 0.02$ in the GFMD data. The relatively large numerical uncertainty of the minimum location results from the minimum being shallow.

To better resolve the discrepancies between the scaling approach and the numerical data, Figure 3 shows the ratio $\bar{E}_{\mathrm{GFMD}}/\bar{E}_{\mathrm{s}}$ as a function of reduced height. For $\nu < 0.45$, relative errors turn out to be quite insensitive to ν for any h/a. They can be approximated reasonably well with a single Gaussian constructed according to

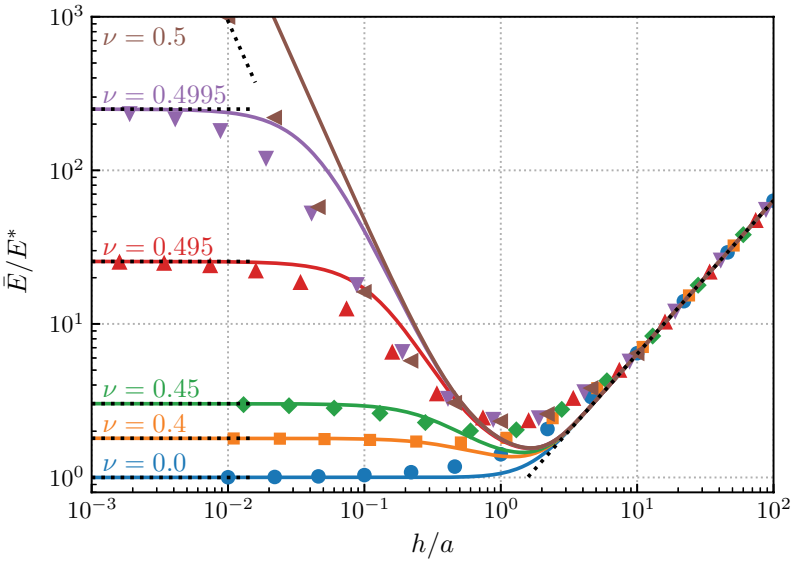

Figure 2. Reduced effective modulus $\bar{E}/E^*$ as a function of the reduced film height h/a for different Poisson's ratios ν. Solid lines are theoretical predictions based on our scaling approach, symbols represent numerical results. Dotted lines indicate the asymptotic limits described in Eq. (21).

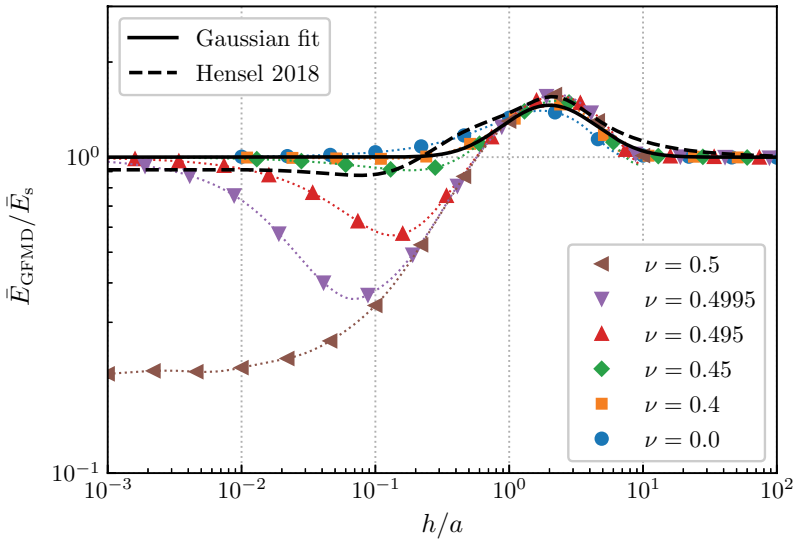

Figure 3. Ratio of numerical and theoretical effective modulus, $\bar{E}_{\mathrm{GFMD}}/\bar{E}_{\mathrm{s}}$. The solid line reflects Eq. (29) and the dashed line represents the empirical fit function from Ref.[3] evaluated for $\nu = 0.495$. Dotted lines are drawn to guide the eye.

$$\frac{\bar{E}_{\mathrm{GFMD}}}{\bar{E}_{\mathrm{s}}} - 1 = A \exp\left\{ -\ln^2\left(\tilde{h}/\tilde{h}_0\right)/\left(2B^2\right)\right\} \tag{29}$$

with $A = 0.46$, $B = 0.75$, and $\tilde{h}_0 = 2$. A similar insensitivity of $\bar{E}_{\mathrm{GFMD}}/\bar{E}_{\mathrm{s}}$ on ν holds for large ν only as long as $h/a \geq 1$. Interestingly, all $\bar{E}_{\mathrm{GFMD}}/\bar{E}_{\mathrm{s}}$ curves almost coincide at $\bar{h}/a = 1$, where they assume the value of $4/3$ within a 3% margin. Unfortunately, the relative errors can exceed a factor of 1.5 for $(h/a)^2 > 1 - 2\nu$ while $h/a \ll 1$. Nonetheless, they always remain below a factor of $\pi^2/2$.

Since previous works[2,3,5,7,21] considered mostly stick conditions for the elastomer-punch interface, comparing our numerical data to existing data or (semi-) empirical approximations for $\bar{E}(h/a)$ may not appear meaningful at first sight. However, we note that the overall trends are similar and that comparisons between different boundary conditions and comparisons between FEM and GFMD data may yet be insightful. We find Hensel *et al.*'s[3] (well, ugly) fit function to match our data most beautifully, which is shown exemplarily for $\nu = 0.495$ in Figure 3, in particular for $0.5 < h/a < 10$. Interestingly, for $h/a < 0.5$, their fit function is close to our analytical result. Thus, it does not capture the minimum associated with the large Poisson's ratios, which may well be because Hensel *et al.* assumed stick conditions between punch and elastomer.

4.2. Pull-off stress

In order to deduce the adhesive pull-off stress $\sigma_p = F_\mathrm{p}/(\pi a^2)$ from $\bar{E}(h/a)$, we replace $\partial \ln \bar{E}/\partial \ln a_\mathrm{c}$ in Eq. (26) with $-\partial \ln \bar{E}/\partial \ln \tilde{h}$ so that

$$\sigma_\mathrm{p} = \sqrt{\frac{4\bar{E}(\tilde{h})\gamma}{a\tilde{h}\left(2 - \partial \ln \bar{E}(\tilde{h})/\partial \ln \tilde{h}\right)}}. \tag{30}$$

The derivatives are evaluated numerically from the GFMD data shown in Figure 2 using cubic spline interpolation. Results for the pull-off stress are shown in Figure 4. To ensure their correctness, the pull-off stresses were also computed for selected values of ν at $h/a = 0.1$ with simulations mimicking tack tests. Agreement was always within 2%. Since direct adhesive simulations are much more demanding and more prone to discretization errors than computations of $\bar{E}$ using non-overlap constraints, we believe the presented results to have errors well below 2%.

Using our analytical expression for $\bar{E}(h/a)$ directly to estimate the pull-off stress turned out to be disappointing. However, using the asymptotic scaling for σ_p yields relatively satisfactory results, because it allows one to transition from $\nu < 0.5$ to $\nu = 0.5$ scaling when crossing over from extreme to large confinement. Likewise, it is beneficial to transition from $\nu = 0.5$ to $h/a \to \infty$ scaling when crossing over from confined to unconfined.

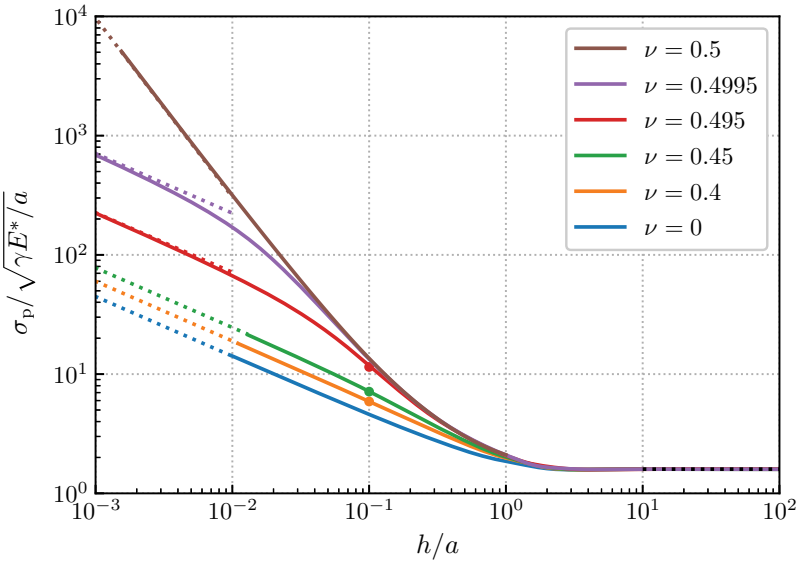

Figure 4. Computed pull-off stress as a function of confinement h/a for a wide range of Poisson's ratios ν. Dotted lines, full lines, and circles represent asymptotic limits, analysis of the numerical $\bar{E}(h/a)$ curves, and results from adhesive GFMD simulations, respectively.

The asymptotic solutions for σ_p can be obtained from Eq. (30) by exploiting once more Eq. (11):

$$\sigma_p = \begin{cases} \sqrt{8\gamma E^*/(\pi a)} & \text{for } h/a \gg 1 & (31a) \\ \sqrt{c_1(\nu)\gamma E^*/\left(a\tilde{h}\right)} & \text{for } h/a \ll \sqrt{1-2\nu} \quad \text{and } \nu < 0.5 & (31b) \\ \sqrt{3\gamma E^*/\left(32ta\,\tilde{h}^3\right)} & \text{for } h/a \ll 1 \quad \text{and } \nu = 0.5. & (31c) \end{cases}$$

Related scaling relations have been proposed before[1,4,7,12,13,15,16,36] for varying boundary conditions (BCs), however, generally assuming $\nu = 0.5$. Historically first, Kendall[15] identified Eq. (31a) for the unconfined system using, as we do, a frictionless elastomer-punch interface. In the opposite limit, $h/a \to 0$, he found $\sigma_p \propto 1/\sqrt{h}$, which differs from our Eq. (31c) because Kendall used a slip condition for the elastomer–substrate interface, while we assumed a stick condition. Yang and Li[36] confirmed Kendall's scaling relation, albeit they corrected the numerical prefactor by multiplying Kendall's result with $\sqrt{E^*/K}$, where K is the bulk modulus. In the case where Yang and Li employ our BCs, they also find Eq. (31c). In fact, Yang and Li considered all four possible combinations of elastomer-punch and elastomer-substrate BCs. However, they only considered $\nu = 0.5$.

4.2.1. Deducing ν from mechanical measurements

In order for our calculations to benefit the determination of the Poisson's ratio from mechanical measurements or, rather that of $\Delta\nu = 0.5 - \nu$, our results for $\bar{E}$ and σ_p are best represented as functions of ν for fixed values of h/a, as is done in Figure 5. This way E^* and/or σ_p only need to be determined once for

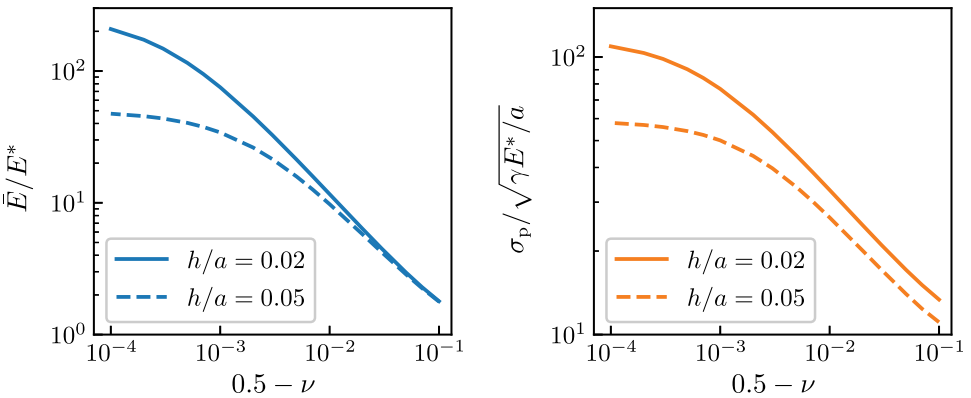

Figure 5. GFMD results for the dimensionless, effective modulus $\bar{E}/E^*$ and the predicted reduced pull-off stress $\sigma_p/\sqrt{\gamma E^*/a}$ for Poisson's ratios $\nu = 0.4999$ to 0.4 for the confinements $h/a = 0.02$ and $h/a = 0.05$.

a semi-infinite elastomer and once more for a confined elastomer. Similar approaches to determine Δv experimentally from $\bar{E}(h/a)$ have already been pursued successfully.[37,38]

Information as that presented in Figure 5 is certainly only beneficial as long as we are not yet too deep in the extreme confinement limit since $\bar{E}$ and σ_p are no longer sensitive to $\log(\Delta v)$ in that regime.

Using very small h/a from the beginning is not necessarily effective either, since it might be equally important and infeasible to accurately align the flat punch as well as to account for the effects arising from the combined compliance of substrate, punch, and driving apparatus. Thus, for Δv suspected to exceed 10^{-3} and 10^{-4}, we would recommend to use $h/a = 0.05$ and $h/a = 0.02$, respectively.

Determining Poisson's ratios of confined layers to less than 10^{-4} might be possible through optical measurements of the bulge arising right next to the indenter.[39] However, we could not identify bulge characteristics, *i.e.*, appropriately undimensionalized bulge widths or heights, which appear to be promising candidates. The thin slit between the indenter and elastomer seems to have the largest sensitivity to $\log(\Delta v)$. Unfortunately, its determination would require extremely smooth surfaces and a high-accuracy measurement of the buried gap.

4.3. Crack formation and propagation

Crack growth during punch retraction becomes stable for sufficiently confined elastomers and large Poisson's ratios, *i.e.*, below a critical film height $h_c(\nu)$. Evaluating the stability condition, Eq. (28), for $\nu = 0.5$, we locate the transition near $h_c(0.5)/a = 3.44$ from the GFMD data and at $h_c(0.5)/a = 3.692$ from our scaling ansatz. As ν decreases, the estimates for $h_c(\nu)/a$ move to smaller values. However, $h_c(\nu)/a$ becomes tedious to evaluate numerically from GFMD data once the elastomer is no longer very close to being incompressible.

Once h/a is well below unity, elastic instabilities, so-called fingering instabilities, occur for (nearly) incompressible elastomers,[4,6–9] which result in wavy displacement fields below the indenter. Their characteristic wave number q was related to a minimum in the stiffness of surface undulations, $\kappa = qE^* c(qh, \nu)/4$.[4,8,10–13] It is located at $q = 2.12/h$ for $\nu = 0.5$ and at $q = 1.553/h$ for $\nu = 0.4$. These values translate to wavelengths of $\lambda = 2.964h$ and $\lambda = 4.046h$, respectively. The minimum moves to larger wavelengths, with further decreasing ν and disappears completely at $\nu = 0.25$.

Simulations[12,13] reveal elastic instabilities similar to those observed experimentally, thereby supporting the theoretical analysis. It yet seems unclear why and how the simulated patterns in two-dimensional contacts[13] break the

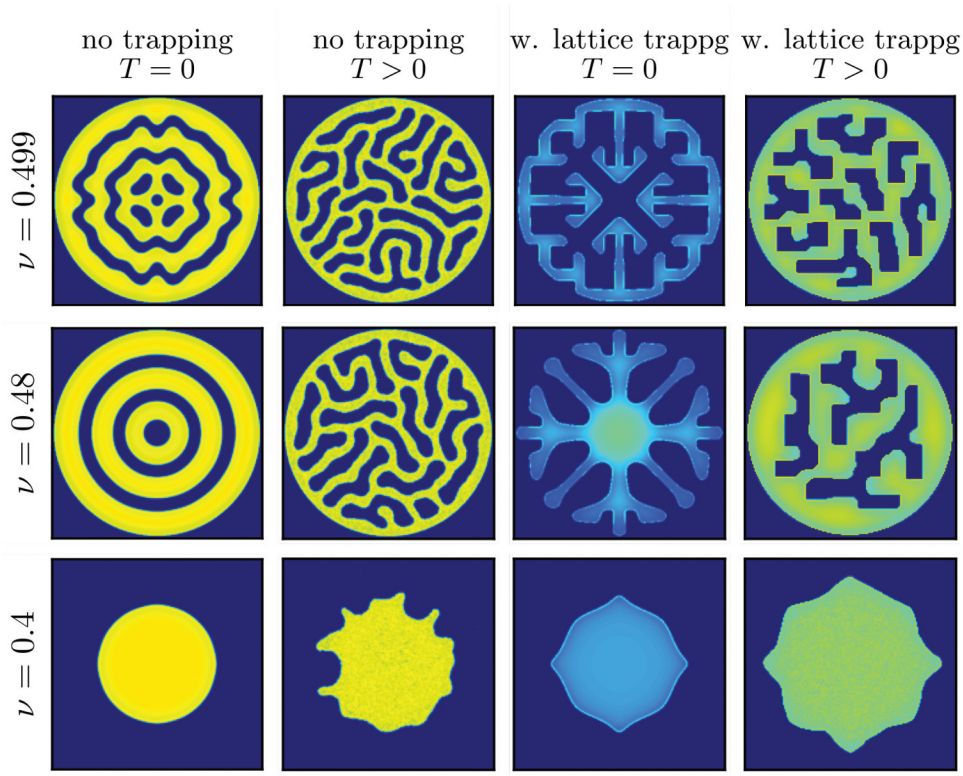

Figure 6. Stress heat maps at selected moments during detachment for a confined elastomer with reduced height $h/a = 0.06$. Bright colors indicate high stress, black represents non contact. Poisson's ratios are kept constant in each row and take the values $\nu = 0.499, 0.48, 0.4$ from top to bottom. Columns differ in the way how continuum mechanics is terminated at the small scale, *i. e.*, with and without thermal noise, and with and without lattice trapping.

symmetry of the mathematical problem, which has circular symmetry in the absence of discretization and periodic boundary conditions. To elucidate this issue further, we simulated the detachment process for three different Poisson's ratios using different ways in which the continuum model was terminated at small scales. Some of the most intriguing snapshots taken during detachment are compiled in Figure 6.

Every graph in a row in Figure 6 reflects the same continuum model in that ν and h/a is kept constant. However, they differ in terms of their discretization – leading to or suppressing lattice trapping at small scales – and in terms of the absence or presence of random noise, which is introduced with a Langevin thermostat. Despite representing the same continuum limit, all four graphs within a row look qualitatively different with the exception of the two right panels in the bottom row, which are both singly connected contact domains with the four-fold symmetry of the discretized model.

The most highly symmetric patterns are obtained when thermal noise and lattice trapping are absent. While the $\nu = 0.4$ and $\nu = 0.48$ systems have circular symmetry, the $\nu = 0.499$ configuration reduces to a four-fold symmetry axis. The symmetry reduction is not due to the presence of periodic boundary conditions in our square domain but results from the discretization of the elastomer's surface into grid points forming a square lattice. We come to this conclusion because increasing the buffer between the punch and the boundary of the simulation cell does not change the point at which circular symmetry is broken. However, we observed that the rate of retraction can matter. For example, a complete loss of symmetry can occur even in the absence of thermal noise when decreasing from very small to extremely small retraction rates. Since our four-fold symmetry axis is only broken by the order in which numbers are added up, the complete loss of symmetry can only result from an accumulation of round-off errors. We suspect that a similar round-off error progression to significant digits is responsible for the low-symmetry configurations produced by Gonuguntla *et al.*,[13] owing to them using a highly efficient conjugate gradient minimization method and/or because computers used smaller data precision in 2006 than they do nowadays. Given our results, we predict that instability patterns assume a quasi-circular symmetry, when elastomers are retracted quickly if the original surfaces are sufficiently planar.

Switching on temperature yield configurations similar to those observed experimentally and more so for a fine discretization avoiding lattice trapping. Specifically, the snapshots shown in the "no-trapping, $T > 0$" column resemble typical experimental images[4,6–9] for $\nu > 0.45$ and the contact shown for $\nu = 0.4$ in that column is similar to that depicted in Fig. 9a of Ref.[8] for $\nu = 0.4$. Due to lattice trapping, the non-contact patches show 90 ° corners oriented w. r.t. the microscopic shape, similar to but substantially stronger than in the pioneering simulations by Gonuguntla *et al.*,[13] who thus must have also discretized their domain into squares.

In the presence of thermal noise, the width of contact and of non-contact domains is similar in size. Their combined width indeed satisfies $\lambda \approx 3h$, which is the expected wavelength for nearly incompressible elastomers introduced at the beginning of this section. However, contact generally appears broader than non-contact due to (close-to) circular symmetry. This difference might matter for a comparison between single-wavelength pen-on-paper theory and real or realistic patterns. In addition, the surface tension can shift the characteristic wavelength to larger values.[9,13]

We also analyze the effect of lattice trapping. For this phenomenon to occur, it does not matter whether the range of adhesion is decreased at fixed discretization $\Delta x = \Delta y$ or the mesh size is increased at fixed range of adhesion, as long as Δx is clearly less than typical contact and non-contact widths. Lattice

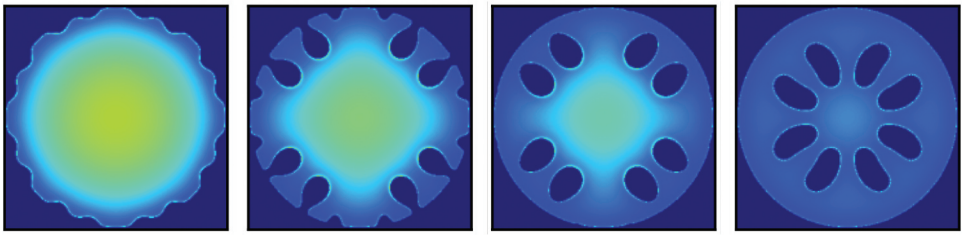

Figure 7. Stress heat maps showing the nucleation of edge cracks and their motion toward the punch center. The number of time steps between subsequent images were 9000, 2000 and 14000 from left to right.

trapping also counteracts symmetry reduction, as revealed most clearly in the bottom row of Figure 7, where thermal fluctuations are no longer strong enough to roughen the contact line during the course of the simulation. In other words, symmetry reduction can become an activated process in the case of lattice trapping whereby contact domains become thicker than non-contact regions upon retraction.

Unfortunately, our simulations do not correlate very well with some experiments regarding one aspect: for $\nu > 0.45$, we usually observe the nucleation of non-contact below the punch center, while experiments often find finger-shaped non-contact regions to emerge from the rim of the punch and then to move inward.[4,6–8]

Reasons for this discrepancy might be (i) the simulations ignore the effect of air pressure, which certainly favors the primary detachment to occur at the contact edge, (ii) the simulations neglect shear stress, which can be large near the contact periphery, (iii) no attempts were made to model viscoelastic effects, and (iv) the edge singularities in the normal stress are cut off too early due to a coarse discretization. Nonetheless, other experiments observed, as we did, crack nucleation in the center,[9,11,13,38] especially in cases where $h/a \ll 0.1$.

It is beyond the scope of this work to test all four hypotheses for why our non-contact domains nucleate in the centerin particular, as testing the first three does not fall into the realm of our model. However, we did investigate the fourth hypothesis by increasing the resolution from our default value to 4096×4096 for a $h/a = 0.1$ punch and $\nu = 0.495$ elastomer while decreasing the range of adhesion and the rate of retraction so that the ratio of local elastic stiffness and maximum curvature of the tensile potential remained constant. As a consequence, the detachment nucleates at the periphery of the contact as is revealed in Figure 7 for the fine discretization, while it nucleated in the center for the coarser simulation.

5. Summary

In this work, we combine and streamline existing approaches to the mechanics of confined elastomers interacting with a flat punch. In doing so, we identify a relatively simple, yet physically motivated expression for how the effective modulus of the confined layer, $\bar{E}$, depends on its Poisson's ratio ν and the ratio of elastomer height and punch radius h/a. Using our approach, the Poisson's ratios no longer have to be close to 0.5. One consequence of this is that large confinement can be distinguished from extreme confinement, for which deviations from ideal incompressibility cannot be ignored. A central benefit of the pursued scaling ansatz is that the asymptotic dependence of $\bar{E}(h/a \to 0)$ allows the simulated pull-off force to be estimated reasonably well for any combination of ν and h/a. Of course, in real-laboratory experiments, the compliance of the substrate, the indenter, or, more generally speaking, the system must be considered when deducing $\bar{E}$ in the extreme-confinement limit. Moreover, eliminating viscoelastic retardation implies (unrealistic?) requirements on the patience of experimentalists.

The central assumption of the analytical part of our study is that the elastic energy of a confined elastomer stems predominantly from surface undulations with wavelengths in the vicinity of the punch radius. This leads to a closed-form expression in Eq. (10) for $\bar{E}(h/a)$ with two parameters of order unity, whose precise value can be fixed by demanding the asymptotic limits of $h/a \to 0$ and $h/a \to \infty$ to be exactly reproduced. The pursued treatment can be repeated for boundary conditions (BCs) other than ours, which is a slip BC between the elastomer-punch interface and a stick BC for the elastomer–substrate interface. In these cases, the relation for the stiffness of the surface undulation of the wave vector q has to be derived or looked up in the literature,[11,27–29,36] *i.e.*, the replacement of Eq. (2). All remaining steps to estimate $\bar{E}(h/a)$ for other BCs can certainly be done by repeating the procedures worked out in this study. However, if both interfaces have slip boundary conditions, qualitatively different behavior ensues and other scaling relations apply than in the remaining three cases.[20,36] Investigating those is beyond the scope of this paper.

The analytical calculations are augmented with Green's function molecular dynamics (GFMD) simulations. They yield accurate reference data for the reduced elastic modulus and pull-off force as functions of reduced height and Poisson's ratios. In particular, the latter can be useful to determine experimentally the deviation of ν from $\nu = 0.5$.

The GFMD simulations also reveal that the initiation and the formation of cracks that occur during stable crack growth depend sensitively on the way in which continuum mechanics is terminated at small scales. For example, the (effective) range of interaction can determine whether cracks initiate from the punch center or from its periphery. Moreover, if

interactions are so short ranged that lattice pinning ensues, small-scale features of the substrate, *e.g.* its crystallinity, can be reflected in the crack at coarse scales.

Acknowledgements

We thank René Hensel for stimulating discussions.

Disclosure statement

No potential conflict of interest was reported by the author(s).

References

[1] Gent, A. N. Fracture Mechanics of Adhesive Bonds. *Rubber Chem. Technol.* 1974, *47*(1), 202–212. DOI: 10.5254/1.3540427.
[2] Ganghoffer, J. F.; Gent, A. N. Adhesion of a Rigid Punch to a Thin Elastic Layer. *J. Adhes.* 1995, *48*(1–4), 75–84. DOI: 10.1080/00218469508028155.
[3] Hensel, R.; McMeeking, R. M.; Kossa, A. Adhesion of a Rigid Punch to a Confined Elastic Layer Revisited. *J. Adhes.* 2018, *95*(1), 44–63. DOI: 10.1080/00218464.2017.1381603.
[4] Webber, R. E.; Shull, K. R.; Roos, A.; Creton, C. Effects of Geometric Confinement on the Adhesive Debonding of Soft Elastic Solids. *Phys. Rev. E - Stat. Phys. Plasma. Fluid. Relat. Interdiscip. Top.* 2003, *68*(2), 11.
[5] Shull, K. R.; Ahn, D.; Chen, W.-L.; Flanigan, C. M.; Crosby, A. J. Axisymmetric Adhesion Tests of Soft Materials. *Macromol. Chem. Phys.* 1998, *199*(4), 489–511. DOI: 10.1002/(SICI)1521-3935(19980401)199:4<489::AID-MACP489>3.0.CO;2-A.
[6] Crosby, A. J.; Shull, K. R.; Lakrout, H.; Creton, C. Deformation and Failure Modes of Adhesively Bonded Elastic Layers. *J. Appl. Phys.* 2000, *88*(5), 2956–2966. DOI: 10.1063/1.1288017.
[7] Shull, K. R.; Flanigan, C. M.; Crosby, A. J. Fingering Instabilities of Confined Elastic Layers in Tension. *Phys. Rev. Lett.* 2000, *84*(14), 3057–3060. DOI: 10.1103/PhysRevLett.84.3057.
[8] Shull, K. R.; Creton, C. Deformation Behavior of Thin, Compliant Layers under Tensile Loading Conditions. *J. Polym. Sci. Part B Polym. Phys.* 2004, *42*(22), 4023–4043. DOI: 10.1002/polb.20258.
[9] Ghatak, A.; Chaudhury, M. K. Adhesion-induced Instability Patterns in Thin Confined Elastic Film. *Langmuir*. 2003, *19*(7), 2621–2631. DOI: 10.1021/la026932t.
[10] Sharma, A.; Ghatak, A.; Chaudhury, M.; Shenoy, V. Meniscus Instability in a Thin Elastic Film. *Phys. Rev. Lett.* 2000, *85*(20), 4329–4332. DOI: 10.1103/PhysRevLett.85.4329.
[11] Mönch, W.; Herminghaus, S. Elastic Instability of Rubber Films between Solid Bodies. *Europhys. Lett.* 2001, *53*(4), 525–531. DOI: 10.1209/epl/i2001-00184-7.
[12] Sarkar, J.; Shenoy, V.; Sharma, A. Patterns, Forces, and Metastable Pathways in Debonding of Elastic Films. *Phys. Rev. Lett.* 2004, *93*(1), 1457–1469. DOI: 10.1103/PhysRevLett.93.018302.

[13] Gonuguntla, M.; Sharma, A.; Sarkar, J.; Subramanian, S. A.; Ghosh, M., and Shenoy, V. Contact Instability in Adhesion and Debonding of Thin Elastic Films. *Phys. Rev. Lett.* 2006, *97*(1 018303).
[14] Sneddon, I. N. The Relation between Load and Penetration in the Axisymmetric Boussinesq Problem for a Punch of Arbitrary Profile. *Int. J. Eng. Sci.* 1965, *3*(1), 47–57. DOI: 10.1016/0020-7225(65)90019-4.
[15] Kendall, K. The Adhesion and Surface Energy of Elastic Solids. *J. Phys. D: Appl. Phys.* 1971, *4*(8), 1186–1195. DOI: 10.1088/0022-3727/4/8/320.
[16] Chung, J. Y.; Chaudhury, M. K. Soft and Hard Adhesion. *J. Adhes.* 2005, *81*(10–11), 1119–1145. DOI: 10.1080/00218460500310887.
[17] Lindsey, G. H.; Schapery, R. A.; Williams, S. M. L.; Zak, A. R. The Triaxial Tension Failure of Viscoelastic Materials. Technical Report 63–152, Aerospace Research Laboratories, 1963.
[18] Lindsey, G. H. Triaxial Fracture Studies. *J. Appl. Phys.* 1967, *38*(12), 4843–4852. DOI: 10.1063/1.1709232.
[19] Lai, Y. H.; Dillard, D. A.; Thornton, J. S. The Effect of Compressibility on the Stress Distributions in Thin Elastomeric Blocks and Annular Bushings. *J. Appl. Mech. Trans. ASME*. 1992, *59*(4), 902–908. DOI: 10.1115/1.2894059.
[20] Lin, Y. Y.; Hui, C. Y.; Conway, H. D. Detailed Elastic Analysis of the Flat Punch (Tack) Test for Pressure-sensitive Adhesives. *J. Polym. Sci. Part B Polym. Phys.* 2000, *38*(21), 2769–2784. DOI: 10.1002/1099-0488(20001101)38:21<2769::AID-POLB60>3.0.CO;2-J.
[21] Sarkar, J.; Sharma, A.; Shenoy, V. Adhesion and Debonding of Soft Elastic Films: Crack Patterns, Metastable Pathways, and Forces. *Langmuir*. 2005, *21*(4), 1457–1469. DOI: 10.1021/la048061o.
[22] Menga, N.; Afferrante, L.; Carbone, G. Effect of Thickness and Boundary Conditions on the Behavior of Viscoelastic Layers in Sliding Contact with Wavy Profiles. *J. Mech. Phys. Sol.* 2016, *95*, 517–529. DOI: 10.1016/j.jmps.2016.06.009.
[23] Menga, N. Rough Frictional Contact of Elastic Thin Layers: The Effect of Geometrical Coupling. *Int. J. Solids Struct.* 2019, *164*, 212–220. DOI: 10.1016/j.ijsolstr.2019.01.005.
[24] Menga, N.; Carbone, G., and Dini, D. Exploring the Effect of Geometric Coupling on Friction and Energy Dissipation in Rough Contacts of Elastic and Viscoelastic Coatings. *J. Mech. Phys. Sol.* 2021, *148* 104273 .
[25] Shenoy, V.; Sharma, A. Stability of a Thin Solid Film with Interactions, 2000. arXiv: cond-mat/0005324.
[26] Campañá, C.; Müser, M. H. Practical Green's Function Approach to the Simulation of Elastic Semi-infinite Solids. *Phys. Rev. B*. aug 2006, *74*(7), 075420. DOI: 10.1103/PhysRevB.74.075420.
[27] Carbone, G.; Mangialardi, L. Analysis of the Adhesive Contact of Confined Layers by Using a Green's Function Approach. *J. Mech. Phys. Solids*. 2008, *56*(2), 684–706. DOI: 10.1016/j.jmps.2007.05.009.
[28] Greenwood, J. A.; Barber, J. R. Indentation of an Elastic Layer by a Rigid Cylinder. *Int. J. Solids Struct.* 2012, *49*(21), 2962–2977. DOI: 10.1016/j.ijsolstr.2012.05.036.
[29] Venugopalan, S. P.; Nicola, L.; Müser, M. H. Green's Function Molecular Dynamics: Including Finite Heights, Shear, and Body Fields. *Model. Simul. Mater. Sci. Eng.* 2017, *25*(3), 0–13. DOI: 10.1088/1361-651X/aa606b.
[30] Bitzek, E.; Koskinen, P.; Gähler, F.; Moseler, M.; Gumbsch, P. Structural Relaxation Made Simple. *Phys. Rev. Lett.* 2006, *97*(17). DOI: 10.1103/PhysRevLett.97.170201.
[31] Zhou, Y.; Moseler, M.; Müser, M. H. Solution of Boundary-element Problems Using the Fast-inertial-relaxation-engine Method. *Phys. Rev. B*. 2019, *99*(14), 144103. DOI: 10.1103/PhysRevB.99.144103.

[32] Wang, A.; Zhou, Y.; Müser, M. Modeling Adhesive Hysteresis. *Lubricants*. 2021, *9:17*, 02.
[33] Zhou, Y.; Wang, A.; Müser, M. How Thermal Fluctuations Affect Hard-wall Repulsion and Thereby Hertzian Contact Mechanics. *Front. Mech. Eng.* 2019, *5:67*, 12.
[34] Müser, M. H. Single-asperity Contact Mechanics with Positive and Negative Work of Adhesion: Influence of Finite-range Interactions and a Continuum Description for the Squeeze-out of Wetting Fluids. *Beilstein J. Nanotechnol.* apr, 2014, *5*, 419–437. DOI: 10.3762/bjnano.5.50.
[35] Gent, A. N. Compression of Rubber Blocks. *Rubber Chem. Technol.* 1994, *67*(3), 549–558. DOI: 10.5254/1.3538691.
[36] Yang, F.; Zhang, X.; Li, J. C. M. Adhesive Contact between a Rigid Sticky Sphere and an Elastic Half Space. *Langmuir*. feb 2001, *17*(3), 716–719. DOI: 10.1021/la0006162.
[37] Tizard, G. A.; Dillard, D. A.; Norris, A. W.; Shephard, N. Development of a High Precision Method to Characterize Poisson's Ratios of Encapsulant Gels Using a Flat Disk Configuration. *Exp. Mech.* 2012, *52*(9), 1397–1405. DOI: 10.1007/s11340-011-9589-6.
[38] Samri, M.; Kossa, A.; Hensel, R. Effect of Subsurface Microstructures on Adhesion of Highly Confined Elastic Films. *J. Appl. Mech. Trans. ASME*. 2021, *88*(3), 1–9. DOI: 10.1115/1.4049182.
[39] Müller, A.; Wapler, M. C.; Wallrabe, U. A Quick and Accurate Method to Determine the Poisson's Ratio and the Coefficient of Thermal Expansion of PDMS. *Soft Matter*. 2019, *15*(4), 779–784. DOI: 10.1039/C8SM02105H.